

Estimation of Arctic Land-Fast Ice Cover based on Dual-Polarized SENTINEL-1 SAR Imagery

Juha Karvonen¹

¹Finnish Meteorological Institute, PB 503, FI-00101, Helsinki, Finland

Correspondence to: Juha Karvonen (juha.karvonen@fmi.fi)

Abstract. Here a method for estimating the land-fast ice (LFI) extent from dual-polarized SENTINEL-1 SAR mosaics of an Arctic study area over the Kara and Barents Seas is presented. The method is based on temporal cross-correlation between adjacent daily SAR mosaics. The results are compared to the LFI of the Russian Arctic-Antarctic Research Institute (AARI) ice charts. An LFI time series covering the time period from October 2015 to the end of August 2017 computed using the proposed methodology is provided on the FMI ftp server. The time series will be extended twice annually.

1 Introduction

Land-fast ice (also known as shore-fast ice, or shortly as fast ice), here denoted by LFI, is sea ice attached to the coastline, to the sea floor along shallow areas or to grounded icebergs [WMO (2015); Weeks (2010); Lepparanta (2011)]. LFI may either grow in place from the sea water or by freezing drifting ice to the shore [WMO (2015)]. LFI does not move with currents and winds. LFI zone is typically seasonal and depends on ice thickness, topography of the sea floor and islands [Lepparanta (2011)]. On average the fast ice edge is located in the water depth of 10-25 m [Zubov (1945); Divine et al. (2004); Mahoney et al. (2007)]. However, there exists seasonal and inter-annual variability. Based on the numbers given e.g. in [Yu et al. (2014)] LFI area covers approximately 13% of the Northern Hemisphere area of sea ice cover, and thus represents an essential fraction of the Arctic sea ice. LFI zone distance from coast varies from a few meters to several hundreds of kilometers [WMO (2015)]. For practical LFI detection some criteria to detect the LFI areas need to be fixed. In [Mahoney et al. (2005)] two criteria have been used for LFI: the ice is contiguous with land and it lacks detectable motion for approximately 20 days. In the methodology presented here a two-week period without ice motion and contiguousness with land have been used as criteria for LFI.

Long-term changes have been found in the LFI regime. The trend seems to be toward reducing LFI area [Divine et al. (2003); Yu et al. (2014)], later formation and earlier disappearance [Mahoney et al. (2014); Seluyzhenok et al. (2015)] and reduction of the LFI thickness [Polyakov et al. (2003, 2012)]. Although LFI zone only covers a relatively small fraction of overall Arctic sea ice extent, it has particular importance for the coastal systems, e.g. by defining the location of polynyas [Morales Maqueda et al. (2004)]. These facts make monitoring of the LFI zone important, also as a climate change indicator.

In the static parts of the LFI zone (during the long static periods) only thermodynamic ice modeling is necessary as the modeled dynamic part can be omitted for static ice. This will increase the reliability of ice modeling in the static LFI areas,

assuming that the static ice areas can reliably be located, as the uncertainties originating from the ice dynamics will then be excluded.

LFI detection based on different techniques and different instruments have been proposed earlier. Passive microwave (PM) data has widely been used for determining sea ice motion, e.g. in [Agnew et al. (1997); Kwok et al. (1998)], but because of their low spatial resolution (5-50 km) PM data have not much been used for fast ice detection [Fraser et al. (2011)]. Some examples of using PM data for LFI estimation exist e.g. temporal correlation median of AMSR-E imagery was used for LFI detection in [Seluyzhenok (2011)]. High resolution near-infrared imagery from Landsat I and II have been used for identification of Alaska LFI as sea ice contiguous with the coast [Barry et al. (1979); Stringer et al. (1978, 1980)]. A method for estimating LFI using cloudless spectroradiometer (MODIS) data was proposed in [Fraser et al. (2011)], more specifically using a 20-day composite of MODIS imagery of eastern Antarctic coast supported by AMSR-E ASI algorithm [Spreen et al. (2008)] sea ice concentration in the case of unreliable (possibly cloudy) MODIS image composites. In [Kim et al. (2015)] machine learning (Random Forest algorithm) using data from multiple instruments (AMSR-E brightness temperature, MODIS ice surface temperature (IST) and SSM/I (Special sensor microwave/imager) ice velocity) were applied to detect LFI. In the study ice velocity and IST proved to be the most significant factors in LFI detection.

Also different methods utilizing SAR imagery for LFI detection have been proposed. Significant advantages of using SAR imagery are the high resolution, typically from tens to a few hundreds of meters, of SAR imagery and the capability to measure in cloudy or dark (no daylight) conditions. SENTINEL-1 temporal cover in the Arctic is comparable to that of a radiometer (e.g. AMSR-2) data. In [Antonova (1997)] the areas of static ice were determined manually from consecutive SAR images (time series). In [Mahoney et al. (2004, 2005)] LFI is detected based on vector grayscale gradient fields of three subsequent SAR images. The bottom fast ice zone can be identified based on the SAR backscatter magnitude [Eicken et al. (2005); Solomon et al. (2005)] because if there is no ice-water interface the dielectric contrast at the bottom is significantly reduced. Ice drift can also be derived from multi-temporal SAR image pairs over the same area. Such SAR ice drift detection algorithms are typically based on temporal cross-correlation, i.e. cross-correlation between co-registered spatially (partly) overlapping SAR images acquired at different time instants, [Fily and Rothrock (1987)], temporal phase-correlation [Thomas et al. (2008)] or optical flow [Sun (1996)]. From time series of ice drift estimates it is possible to derive the static ice areas which can then be interpreted as LFI, assuming the time series of ice drift at a certain location is long enough. Also SAR interferometry can be used for LFI detection [Mayer et al. (2011); Marbouti et al. (2017)], as the phase difference is random for drift ice and coherent for the static ice fields. In [Karvonen (2012)] the cumulative Baltic sea ice drift estimated from multi-temporal SAR imagery was used for locating the Baltic sea LFI by indicating the areas where no ice motion has occurred within a predefined, long-enough time period (typically around two weeks). In [Karvonen (2014)] temporal cross-correlation minimum was used to locate LFI to aid sea ice concentration estimation. The algorithms proposed in this study are used for creating daily time series of the Kara and Barents Sea LFI extent in high-resolution gradually complementing the existing Arctic LFI time series derivable from Arctic operational ice charts.

2 Study Area, Data Sets and Pre-Processing

2.1 Study area

The study area is located in the Kara and Barents Seas. The study area is shown in Fig. 1. The coordinate system (CS) used in this paper is the polar stereographic projection, with a center longitude of 55°E , reference latitude (latitude of the correct scale) of 70°N and the WGS84 datum. The upper left (UL) and lower right (LR) coordinates in this CS are (northing and easting in meters): $\text{UL} = (-700000, -1100000)$ and $\text{LR} = (-2550000, 1100000)$.

2.2 Russian Ice Charts

The Russian Arctic ice charts are provided weekly by AARI on their web page (the English version on http://www.aari.ru/odata/_d0015.php). They are provided as thematic maps and in SIGRID-3 vector format [JCOMM (2014)] in the polar stereographic projection with the mid-longitude of 90°E . In this study the AARI ice chart thematic maps were reprojected into the polar stereographic projection used in this study and the LFI areas were extracted based on the colormap. In this study 51 AARI ice charts of the period from November 2015 to October 2016, covering a whole year time, were used as reference LFI data for defining the algorithm parameters and evaluating the proposed algorithms. Actually, four AARI ice charts (one ice chart for each month in the period January-April 2016) were used for defining the optimal algorithm threshold parameters, and the remaining 47 ice charts were used for evaluation. The study area was cropped from the weekly reprojected thematic AARI ice chart maps, and the cropped images were converted into binary 1-bit per pixel images in which the LFI areas, appearing as white in the AARI ice chart maps, were mapped to the pixel value one and the rest of the image were mapped to the pixel value zero.

2.3 SENTINEL-1 imagery, SAR Mosaic and their processing

All the available C-band SENTINEL-1 dual-polarized Extra Wide (EW) swath mode level 1 Ground Range Detected Medium resolution (GRDM) data with the HH/HV polarization channels over the study area during the study period (October 2015 - August 2017) were used in this study. The SENTINEL-1 SAR data are publicly available through the Copernicus Science Hub (<https://scihub.copernicus.eu/>). The imagery were preprocessed by applying an incidence angle correction to the HH channel and a combined incidence angle and noise floor correction to the HV channel, for details of this process, see [Karvonen (2017)]. After incidence angle and noise floor corrections the image data were geo-rectified into the polar stereographic projection introduced in Section 2.1. After geo-rectification the imagery were still down-sampled to 500 m resolution and finally the daily mosaics were constructed by overlaying the newer images over the older ones such that at each mosaic grid cell (pixel) the newest SAR data prior to the mosaic time label, which is 12:00 UTC each day here, is available. The mosaics are cumulative, meaning that the new imagery is always overlaid over the previous mosaic and the mosaic was initialized only in the beginning of the mosaicking (in this case in October 2015). In practice the data at a given grid cell location is not older than three days as SENTINEL-1 temporal cover over the European Arctic is good. Separate mosaics for HH and HV channels were constructed. A land mask based on the GSHHG coastline data set [Wessel and Smith (1996)] was applied to the mosaics

to exclude land areas from LFI computation. As an example of SAR mosaics the mosaics for HH and HV channels of March 8, 2016 with the land masking are shown in Fig. 2. Dual-polarized EW mode SENTINEL-1 data are systematically acquired over the European Arctic and Greenland waters by ESA, but over the other Arctic areas a single-polarization (HH) mode is used. Near the upper right corner of the study area there is no dual-polarized SENTINEL-1 EW mode data available. This can also be seen as the black area in Fig. 2.

3 Methodology for estimation of land fast ice areas

The proposed LFI extent estimation algorithm is based on averaging of temporal cross-correlation of pairs of adjacent daily SAR mosaics. The temporal cross-correlation, denoted by C_T , between SAR mosaics of two adjacent days is computed as

$$C_T(r, c, t) = \frac{1}{\sigma(r, c, t)\sigma(r, c, t-1)} \sum_{i, j \in W} (M(r+i, c+j, t) - \mu(r, c, t))(M(r+i, c+j, t-1) - \mu(r, c, t-1)). \quad (1)$$

The indices r and c refer to the pixel location (row and column coordinates), t refers to the day ($t-1$ refers to the previous day of the day t), C_T is computed within a round-shaped window W with a radius R (here $R=3$ has been used) around the pixel at the location (r, c) . $M(r, c, t)$ refers to a mosaic pixel value at the location (r, c) on day t . The means $\mu(r, c, t)$ and standard deviations $\sigma(r, c, t)$ are computed over W . The mosaics of the two adjacent days in the computation of C_T are also always mosaics of the same polarization, either HH or HV.

Similar processing is also performed for both HH and HV SAR polarization channel mosaics. The processing for the HH channel is illustrated in the block diagram in Fig. 3. The processing for the HV channel is similar except that a different threshold T_{HV} instead of T_{HH} is applied. First, the temporal cross-correlations for both the SAR channels between the mosaics of pairs of adjacent days covering the most recent two weeks are computed. Only the cross-correlation grids needed for the LFI extent estimation for a particular day which have not been computed earlier are computed, so typically only one new cross-correlation is needed to be computed if the cross-correlations used for the previous day's LFI extent estimation already exist. To reduce the amount of required computation the cross-correlations are computed only for the mosaic grid cells defined by a mask indicating the potential areas of LFI. After computation of the 14 cross-correlation grids, a pixel-wise temporal averaging is performed for them, then a thresholding (with a predefined threshold T_{HH}) is applied to the resulting averaged grid, and finally a morphological opening operator followed by removal of LFI segments smaller than a given number of pixels are applied to the binary grid resulting from the thresholding. The resulting binary grid is a nominal LFI estimate for the HH SAR channel. A similar procedure is performed for the HV SAR channel with the exception of using a threshold value T_{HV} instead of T_{HH} . Finally, the HH and HV channel nominal results are combined by applying a logical AND operator to the HH and HV grids.

To increase the computation performance and to exclude areas where LFI does not appear a mask indicating the potential LFI zone as the areas 100 km or less from the coastline (including islands) was produced. The mask was produced iteratively starting from the coastline, indicated by the land mask, then the distance was iteratively increased by 500 m (pixel size) for the vertical and horizontal neighbor pixels and by $\sqrt{2} \times 500$ m for the diagonal neighbor pixels of the pixels with a distance from

the coast already assigned to them. This was iterated until there were no more distances less than 100 km (corresponding to 200 grid pixels). The use of the proposed mask did not have any effect on the LFI detection and it is used here just to fasten the processing. The execution time for a single day LFI estimation is not very long (some minutes), but for longer LFI time series the difference of execution times with the mask and without the mask is significant, and therefore the mask has systematically

5 been applied in this study. The masking applied here is a very simple approach and in some other areas a more sophisticated mask taking into account the bathymetry e.g. using a given distance from the depth of 25 m, might be more useful. The mask applied is shown in Fig. 4. Unfortunately FMI did not have very accurate bathymetry data over the study area at its disposal and only this simple mask was applied here. With a more accurate mask possibly more time could be saved in computation of LFI time series.

10 For the areas defined by the distance mask, i.e, white areas in Fig. 4 C_T between two adjacent daily mosaics is also first computed. Then the temporal 14 day average of the daily C_T grids are computed. The areas where C_T is close to one (higher than 0.95) are excluded from the average computation, as they represent areas where the mosaic has not updated since the previous day. For SAR data from two different SAR images C_T is in practice always less than one, and even less than 0.95, which is used as a threshold here, because of the speckle present in all radar imagery C_T is decreased even for a static object.

15 C_T is computed in a similar manner for both SAR HH and HV channels. The initial decision whether a pixel represents LFI or doesn't is made based on thresholding of the T_C average. The thresholds for the HH and HV SAR channels were studied by varying the threshold value and then comparing the LFI area detected by thresholding and LFI area of four AARI ice charts of the period January-April 2016, one ice chart for each month. The optimal thresholds were defined by minimizing the estimation error, i.e. the sum of LFI not detected by the algorithm and non-LFI classified to LFI by the algorithm when

20 compared to the AARI ice chart LFI. The optimal thresholds yielded were $T_{HH}=0.31$ and $T_{HV}=0.24$ for HH and HV channel mosaics, respectively. The classification error as a function of C_T for both the channels can be seen in Fig. 5. These curves can be used for deriving the thresholds T_{HH} and T_{HV} . Here we have applied a criterion minimizing the total classification error but also other criteria, depending on the objective, could be considered. A grid cell is considered as possible LFI if the channel-wise cross-correlation averages $\overline{C}_T^{HH} > T_{HH}$ and $\overline{C}_T^{HV} > T_{HV}$, they are adjacent to land (i.e. the LFI segment is

25 connected to any land mask pixel), and they are in the area defined by the distance mask (white areas of Fig. 4). After applying the thresholding a morphological opening operation (i.e. an erosion operation followed by a dilation operation) by a disk with a radius of two pixels to remove narrow elongated high \overline{C}_T segments and small single patches is applied. Narrow elongated segments may appear due to the boundaries of SAR frames over open water, where the incidence angle correction often fails because of varying wave conditions in different SAR frames in a mosaic, and small single patches typically represent errors

30 caused by small singular targets, such as big ships or icebergs. After applying the morphological opening operator removal of small LFI segments is applied. This small segment filtering performs removal of segment smaller than a given threshold value (T_s), here the value $T_s = 100$ pixels, corresponding to an area of 25 km², has been applied. This post-filtering also efficiently reduces the number small erroneous segments due to SAR artifacts and speckle. The same procedure is performed for the HH and HV SAR channels with the only difference of applying a different threshold value (T_{HH} or T_{HV}) depending on the SAR

35 channel in thresholding of the temporal cross-correlation average. Then the LFI estimation results of the two SAR channels

are combined by applying a logical AND operator between the channel-wise classification results. Finally, areas which are not connected (in the sense of 8-pixel neighborhood) to land area defined by the land mask are excluded from the LFI class. This is in practice performed by applying a recursive flood-fill algorithm [Hearn and Baker (1997)] testing the filled pixel neighbors for land (land mask pixels) while filling each contiguous LFI candidate segment produced by the earlier preliminary classification. This result is referred here as method A, shortly FMI-A.

To further reduce the erroneous non-LFI classification to the LFI category by FMI-A, an additional two-week (14 days) temporal logical AND operation applied to fourteen adjacent day FMI-A products is performed. The result after the logical AND operation is referred here as method B (FMI-B).

4 Results

The results were first computed for a test data set over a one year a period from November 2015 to November 2016, and the results were compared with the weekly AARI ice charts. The comparison was pixel-based and it was performed between the daily LFI products and the corresponding AARI LFI of the same date (ice chart issuing date). The daily LFI products are the LFI estimates produced by FMI-A and FMI-B using the mosaic of the LFI product issuing date and mosaics of the preceding two week time period. Totally 47 weekly AARI ice charts were used in the comparison (the exact period was from November 3 2015 to November 1 2016). Four weekly AARI ice charts used in defining the algorithm thresholds were excluded from the numerical comparisons. Because FMI-A also suggested a little amount of LFI during the summer, and these summer LFI areas were the same areas for both the summers included in the study, the summer LFI areas suggested by FMI-A in August 2016 were filtered out (subtracted) from all the FMI-A and FMI-B products. It was assumed that these summer LFI detections were due to inaccuracies in the land mask.

The results of the comparison of FMI-A and FMI-B LFI to AARI ice chart LFI can be seen in Table 1. In the first column are the fractions (in percents) of the LFI classified correctly when compared to AARI ice chart grids for FMI-A and FMI-B, and in the second column are the relative amounts (with respect to the AARI ice chart LFI extent) of grid points, which are not LFI according to the AARI ice charts but classified to LFI by the proposed algorithms. In the parentheses are the standard deviations over all the weekly cases included in the comparison. It can be seen that FMI-A is able to locate over 73% of the LFI indicated by the AARI ice charts, and in addition some over 20%, compared to the AARI LFI area, of LFI areas were suggested by FMI-A. FMI-B only detects some over half of the LFI suggested by the AARI ice charts, but very few areas outside the AARI ice chart LFI area are classified to LFI by FMI-B. An example of the LFI extent based on the cropped AARI ice chart of March 8, 2016 in Fig. 6 and FMI-A and FMI-B LFI estimates of March 8, 2016 are shown in Fig. 7. It can be seen that basically AARI ice chart LFI and FMI-A cover the same areas, but there are some differences near the edges of the detected LFI area. This kind of differences occur in most of the cases, at least partly explaining the differences in classification rates in Table 1. FMI-B detects less LFI than present in the AARI ice chart, but still the LFI ice locations agree well.

Also monthly comparisons between the AARI ice chart LFI and FMI-A and FMI-B LFI were made. The results show that the FMI-A LFI estimates covered about 80% of the AARI LFI during the winter months (January-April, November-December)

and some less (60-70%) during the spring and summer months. Also the amount of FMI-A false detections was increased towards the summer (up to over 40% of the AARI LFI cover in July). For FMI-B the amount of false detection remained low for the whole year, but the amount of FMI-B detections matching with AARI ice chart LFI also decreased towards summer, and was very low in July. On the other hand the total amount of LFI in July was also low and this does not have a large effect
5 on the total classification percentage with respect to the AARI ice chart LFI. The monthly classification results and the relative amount of LFI (fraction of total number of AARI ice chart LFI pixels) are shown in Fig. 8.

For comparing the LFI extent evolution in time the weekly LFI extent over the whole study area during the one-year period corresponding to the AARI ice charts used in this study were computed. These results can be seen in Fig. 9. The FMI-A LFI extent follows the AARI ice chart LFI extent quite well having some larger temporal variations. In the spring the FMI-A LFI
10 extent first decreases some faster (in April 2016) than AARI LFI but later in the melting period (in May 2016) FMI-A decrease becomes slower compared to the AARI LFI extent. FMI-B systematically gives significantly smaller LFI extent estimates, approximately 70% of the corresponding AARI and FMI-A LFI extent throughout the whole one year period.

In Fig. 10 LFI extent time series for both FMI-A and FMI-B over the whole study period are shown. According to FMI-A the maximum LFI extent over the study area was around 170000 km² during the winter 2015-2016 and over 180000 km² during
15 the winter 2016-2017. The LFI maximum in 2016-2017 was reached later than in 2015-2016. This can be explained based on the weather conditions making 2016-2017 a more severe ice winter and having a colder spring than 2015-2016. For the FMI-B LFI extent time series the LFI extent estimates are approximately 70% of the FMI-A LFI extent and the evolution of the time series is in general similar to that of FMI-A.

The LFI time series were compared to air temperature measurements at Longyearbyen weather station in Svalbard (78.22°N,
20 15.63°E) provided by Met.Norway on <http://www.yr.no>. As the Russian weather station measurements were not available, the Longyearbyen air temperatures were used here as a general indicator of the winter severity over the whole study area. During the winter 2015-2016 the average air temperatures were close to -5 degrees (centigrade) until late February 2016 and then decreased to -10 degrees and below. This colder period lasted until mid-April 2016. After this the temperature warming started and average temperature of zero degrees was reached in mid-May 2016. During the winter 2016-2017 the average air
25 temperature dropped below zero in Mid-November 2016 and was then above or around -5 degrees, except for a short cold period in early December 2016, until early January 2017. Then the average air temperature dropped to around -10 degrees and this colder period lasted until mid-April 2017. After mid-April there was still a period of about one month with the average temperatures clearly below zero (around -5 degrees) and the warming started during the second half of May 2017. When
30 comparing the winters 2015-2016 and 2016-2017 the effect of the air temperature on LFI can be seen. The fast growth due to the cold period in the beginning of the winter 2016-2017 can be seen and also the total LFI extent of 2016-2017 is larger due to the longer cold period in the mid-winter and later warming, compared to the winter season 2015-2016.

The LFI of the sub-regions of southwestern Kara Sea, northeastern Kara Sea and Gulf of Ob are also shown in Fig. 10. The fast ice grows most rapidly in the Gulf of Ob and quite slowly in the southwestern Kara Sea during both 2015-2016 and 2016-2017. Also the LFI melt in the Gulf of Ob is fast when compared to the other two areas presented. This is probably due

to the flowing water coming along the river Ob. These annual variations can be compared to those of Fig. 2 in [Divine et al. (2004)].

Also the LFI extent fraction (in percents) for FMI-A and FMI-B at each grid cell over the one year period from November 2015 to October 2016 was computed in a similar manner as in [Fraser et al. (2012)]. For comparison the corresponding fraction was computed also for the weekly AARI ice chart LFI extent of the same one year time period. These numbers also indicate the annual duration of the LFI at each grid cell and are given as percentages of the one year time period in Fig. 11. The results for the whole time period from October 2015 to August 2018 were quite similar, except that the percentages were some higher because part of the summer period of 2017 (with no or very little LFI) was not present in the time series covering the whole study period. The results of the AARI ice chart LFI extent and FMI-A LFI extent are quite similar. In some areas there are minor differences but in general AARI ice chart LFI fraction and FMI-A LFI fraction are in good agreement. On the other hand, FMI-B with the parametrization used here (optimal thresholds T_{HH} and T_{HV}) underestimates the LFI extent fraction compared to AARI ice chart LFI extent, but still the same LFI areas are captured, only with a shorter duration of LFI according to FMI-B.

5 Discussion and Conclusions

In this study an algorithm for detecting LFI over a test area in the Kara and Barents seas using daily SENTINEL-1 dual-polarized SAR mosaics was developed. Both SAR channels (HH and HV) were used jointly for reliably estimating the LFI area. Two versions of the algorithm were presented: FMI-A applies the optimal thresholds for SAR HH and HV channels and after some post-processing combines the channel-wise LFI estimates, in FMI-B an additional multi-temporal logical operation (logical AND) is performed to increase the reliability of the LFI detection. As a result FMI-B makes very little misclassifications, compared to the AARI ice chart LFI extent, in mapping non-LFI grid points to the LFI class, with the cost of reduced LFI detection rate. FMI-B can then be considered as an algorithm locating the LFI areas with a high confidence. Daily LFI extent estimates for a period from October 2015 to August 2017 were generated. The results were also evaluated against weekly Russian AARI ice charts and the correspondence was found to be at an acceptable level, especially when comparing the LFI extent time series. During the melting season the difference between AARI ice chart LFI and FMI-A LFI is some larger than during the freeze-up and mid-winter periods, and this can be seen in both the classification error and the ice extent time series. According to this study the proposed algorithm is suitable for operational LFI monitoring. It should be noted here that AARI ice charts are typically based on satellite image analysis (SAR and optical/IR) of a few days prior to the assigning date of the ice chart and the proposed algorithms use SAR data over a two-week period prior to the issuing date, and due to the different time spans of the input data differences between the LFI estimates may also appear.

In this study the optimal threshold were used for both FMI-A and FMI-B. By using these settings FMI-B is very reliable in that sense that it makes very little false LFI detections compared to AARI ice chart LFI. However, then only a little over half of the total AARI LFI is detected by FMI-B. In this sense FMI-A performs significantly better. However, with lower values for the thresholds T_{HH} and T_{HV} FMI-B detects more AARI LFI with the cost of more false LFI detections. For example with the

threshold values $T_{HH} = 0.19$ and $T_{HV} = 0.15$ the 68.6% of the AARI LFI is detected and 37.5% of additional (to AARI) LFI were detected by FMI-B.

Use of temporal cross-correlation average and temporal cross-correlation median in the algorithm produced quite similar results, and because of its faster computation temporal cross-correlation average was selected here instead of temporal cross-correlation median (requiring sorting of the samples). The execution times on a single CPU-core (Intel Xeon 2.5GHz) with a sufficient amount of RAM memory were reasonable also for operational purposes: computation of LFI extent for one daily SAR mosaic takes 2-4 minutes. As the computation can easily be parallelized, LFI extent estimation e.g. for the whole Arctic or Antarctic areas can easily be performed in a reasonable time by dividing the workload to multiple CPU cores. Here a simple mask based on iteratively estimated distance from land was used to reduce the area of computation and thus fasten the algorithm execution. This was a very useful feature in computing longer time series; the execution time was reduced to less than half of the execution time without using the mask.

Compared to other LFI detection methods the proposed method has some advantages. The obvious advantage of using SAR data instead of radiometer data is the significantly higher resolution, and the advantage of using SAR data instead of optical or infrared/near-infrared satellite data (such as MODIS) is the ability of SAR to measure in all conditions independently of clouds or sunlight. LFI can be derived from ice drift based on multi-temporal SAR imagery but estimation of the ice drift is a much more time-consuming process than applying direct temporal cross-correlation. The LFI estimation accuracy of methods based on SAR ice drift is approximately similar to that of LFI-A. Using temporal cross-correlation minimum instead of its average is less robust to local errors than a statistical measure, such as average or median, as it is based only on one value. Methods based on SAR segmentation and SAR backscattering have several potential error sources: C-band SAR backscattering is dependent on the ice surface roughness, which may vary for LFI, SAR backscattering is also dependent on the SAR incidence angle which varies for different acquisitions of a fixed location, and wet snow cover has a significant effect on SAR backscattering making algorithms directly based on SAR backscattering unreliable, especially during the melting season.

An LFI product covering the whole Arctic and Antarctic based on SENTINEL-1 is also technically feasible. There is one limitation related to the SENTINEL-1 acquisition mode: over most of the Arctic SENTINEL-1 is acquiring EW mode HH polarization only and the dual-polarized data are acquired only over the European Arctic and Greenland areas. However, it seems that even the HH channel SENTINEL-1 data alone are sufficient for estimating the LFI extent, even though combining the two polarization channels would increase the reliability of the product to some extent. Some preliminary experiments indicated slight increase of false LFI classification compared to AARI ice charts when using HH channel data alone, the amount of correctly detected LFI remained approximately the same as for the combined HH and HV channel classification.

One major problem in establishing an operational Arctic/Antarctic LFI service is the vast amount of daily SENTINEL-1 data and the current limited resources in data transmission and storage.

According to FMI-A there seemed to be LFI even during the summer (late August). The same areas were classified to LFI by FMI-A in both the summers included in this study. This summer LFI naturally is a classification error in the study area, and those few areas indicated as LFI by FMI-A are typically areas very close to the coastline, and thus very likely due to inaccuracies in positioning of the land mask, causing land or mixed pixels to be included in the temporal cross-correlation

computation. To exclude these areas the LFI detected by FMI-A in late-August 2016 were filtered out (subtracted) from all the FMI-A and FMI-B LFI extent maps.

Future plans include to continue computing a time series of daily LFI over the study area and update the LFI data set twice annually, once in spring and once in autumn. The data will be provided to interested parties through the FMI ftp in GeoTIFF (thematic map) and NetCDF (numeric data) formats.

Also ways to further improve the current algorithms need to be studied. Some interesting alternatives for future algorithm development are the use of varying thresholds according to the time of the year or weather data, and applying a dual-threshold temporal cross-correlation average thresholding scheme, i.e. first applying a lower threshold, then applying a higher threshold and finally combining the two results in an optimal way. Also a combination of applying FMI-B and FMI-A could be studied. This combination could first locate the LFI with high confidence (FMI-B) and then extend the FMI-B LFI extent based on the FMI-A result.

References

- Agnew, T.A., H. Le, T. Hirose, Estimation of large scale sea ice motion from SSM/I 85.5 GHz imagery, *Annals of Glaciology*, v. 25, pp. 305-311, 1997.
- Antonova, S., Spatial and temporal variability of the fast ice in the Russian Arctic Master Thesis, State University of St. Petersburg, Russia and University of Hamburg, Germany, St. Petersburg, 2011.
- Barry, R. G., R. E. Moritz, J. C. Rogers, The fast ice regimes of the Beaufort and Chukchi Sea coasts, Alaska, *Cold Regions Science and Technology*, v. 1, n. 2, pp. 129-152, 1979.
- Divine D., R. Korsnes, A. Makshtas, Variability and climate sensitivity of fast ice extent in the north-eastern Kara sea, *Polar Res.*, v. 22, n. 1, pp. 27–34, 2003.
- 10 Divine D., R. Korsnes, A. P. Makshtas, Temporal and spatial variation of shore-fast ice in the Kara Sea, *Continent Shelf Research*, v. 24, n. 15, pp. 1717–1736, doi:10.1016/j.csr.2004.05.010, 2004.
- Eicken H., I. Dmitrenko, K. Tyshko, A. Darovskikh, W. Dierking, U. Blahak, J. Groves, H. Kassens, Zonation of the Laptev Sea landfast ice cover and its importance in a frozen estuary, *Global and Planetary Change*, v. 48, n. 1-3, pp. 55-83, 2005.
- Fily, M. D. A. Rothrock, Sea ice tracking by nested correlations, *IEEE Transaction on Geoscience and Remote Sensing*, v. GE-25, n. 5, pp. 15 570–580, 1987.
- Fraser, A.D., R. A. Massom, K. J. Michael, Generation of high-resolution East Antarctic landfast sea-ice maps from cloud-free MODIS satellite composite imagery, *Remote Sensing of Environment*, v. 114, n. 12, pp. 2888-2896, 2011.
- Fraser, A.D., R. A. Massom, K. J. Michael, B. K. Galton-Fenzi, J. L. Lieser, East Antarctic Landfast Sea Ice Distribution and Variability, 2000–08, *Journal of Climate*, v. 25, n. 4, pp. 1137-1156, 2012
- 20 Hearn D., M. P. Baker, *Computer Graphics*, C version, p. 130, Prentice Hall Press, Upper Saddle River, New Jersey, USA, 1997.
- JCOMM (Joint World Meteorological Organization (WMO) - Intergovernmental Oceanographic Commission (IOC) Technical Commission for Oceanography and Marine Meteorology), SIGRID-3: A vector archive format for sea ice charts, JCOMM Technical Report n. 23, revision 3, 2014.
- Karvonen J., Operational SAR-based sea ice drift monitoring over the Baltic Sea, *Ocean Science*, v. 8, pp. 473-483, (available online 25 <http://www.ocean-sci.net/8/473/2012/os-8-473-2012.html>), DOI :10.5194/os-8-473-2012, 2012.
- Karvonen J., Baltic Sea Ice Concentration Estimation Based on C-Band Dual-Polarized SAR Data, *IEEE Transactions on Geoscience and Remote Sensing*, v. 52, n. 9, pp. 5558–5566, DOI: 10.1109/TGRS.2013.2290331, 2014.
- Karvonen J., Baltic Sea Ice Concentration Estimation Using SENTINEL-1 SAR and AMSR2 Microwave Radiometer Data, *IEEE Transactions on Geoscience and Remote Sensing*, v. 55, n. 5, pp. 2871-2883, DOI: 10.1109/TGRS.2017.2655567, 2017.
- 30 Kim M., J. Im, H. Han, J. Kim, S. Lee, M. Shin, Landfast sea ice monitoring using multisensor fusion in the Antarctic *GIScience & Remote Sensing*, Volume 52, n. 2, pp. 239-256, 2015.
- Kwok R., A. Schweiger, D.A. Rothrock , S. Pang, C. Kottmeier, Sea ice motion from satellite passive microwave imagery assess with ERS SAR and buoy motions. *Journal of Geophysical Research*, v. 103, n. C4, pp. 8191-8214, 1998.
- Lepparanta, M., *The Drift of Sea Ice*, 2nd ed., Springer-Verlag, Berlin-Heidelberg, Germany, 2011.
- 35 Mahoney A., H. Eicken, A. Graves, L. Shapiro, P. Cotter, Landfast sea ice extent and variability in the Alaskan Arctic derived from SAR imagery, *Proc. IEEE International Geoscience and Remote Sensing Symposium Proceedings (IGARSS'04)*, v. 3. pp. 2146-2149, 2004.

- Mahoney, A., H. Eicken, L. Shapiro, A. Graves, Defining and locating the seaward landfast ice edge in northern Alaska, Proc. International Conference on Port and Ocean Engineering under Arctic Conditions (POAC 2005), Potsdam, N.Y., June 26-30, pp. 991-1000, 2005.
- Mahoney, A., H. Eicken, A. G. Gaylord, L. Shapiro, Alaska landfast sea ice: Links with bathymetry and atmospheric circulation, *Journal of Geophysical Research*, v. 112, n. C2, pp. 2156-2202, doi:10.1029/2006JC003559, 2007.
- 5 Mahoney, A. R., H. Eicken, A. G. Gaylord, R. Gens, Landfast sea ice extent in the Chukchi and Beaufort seas: The annual cycle and decadal variability, *Cold Regions Science and Technology*, v. 103, pp. 41–56, doi:10.1016/j.coldregions.2014.03.003, 2014.
- Morales Maqueda M. A., A. J. Willmott, N. R. T. Biggs, Polynya Dynamics: a Review of Observations and Modeling, *Reviews of Geophysics*, v. 42, n. 1, pp. 1944-9208, DOI: 10.1029/2002RG000116, 2004.
- Marbouti M., J. Praks, O. Antropov, E. Rinne, M. Lepparanta, A Study of Landfast Ice with Sentinel-1 Repeat-Pass Interferometry over the Baltic Sea, *Remote Sensing*, v. 9, n. 8, 833; doi:10.3390/rs9080833, 2017.
- Meyer F. J., A. R. Mahoney, H. Eicken, C. L. Denny, H. C. Druckenmiller, S. Hendricks, Mapping arctic landfast ice extent using L-band synthetic aperture radar interferometry, *Remote Sensing of Environment*, v. 115, n. 12, pp. 3029-3043, 2011.
- Polyakov I. V., G. V. Alekseev, R. V. Bekryaev, U. S. Bhatt, R. Colony, M. A. Johnson, V. P. Karklin, D. Walsh, A. V. Yulin, Long-term ice variability in Arctic marginal seas, *Journal of Climate*, v. 16, n. 12, pp. 2078–2085, doi:10.1175/1520-0442(2003)016<2078:Liviam>2.0.CO;2, 15 2003.
- Polyakov I. V., J. E. Walsh, R. Kwok, Recent changes of Arctic multiyear sea ice coverage and the likely causes, *Bulletin of American Meteorological Society*, v. 93, n. 2, pp. 145–151, doi:10.1175/Bams-D-11-00070.1, 2012.
- Selyuzhenok V., Validation of the satellite-based landfast ice mapping, Master Thesis, State University of St. Petersburg, Russia and University of Hamburg, Germany, St. Petersburg, 2011.
- 20 Seluyzhenok V., T. Krumpfen, A. Mahoney, M. Janout, R. Gerdes, Seasonal and interannual variability of fast ice extent in the southeastern Laptev Sea between 1999 and 2013, *Journal of Geophysical Research*, v. 120, n. 13, pp. 7791-7805, doi: 10.1002/2015JC011135, 2015.
- Solomon S. M., G. Manson, D. Monita, T. Hirose, D. Power, Synthetic Aperture Radar Remote Sensing of Bottom Fast ice in the MacKenzie Delta Region, Northwest Territories, Canada, 2005 ArcticNet Annual Conference Proceedings, pp. 96-97, 2005.
- Spreen G., Kaleschke L., Heygster G., Sea Ice Remote Sensing Using AMSR-E 89 GHz Channels, *Journal of Geophysical Research*, v. 113, 25 n. C2, C02S03, DOI: 10.1029/2005JC003384, 2008.
- Stringer W.J., S.A. Barrett, L. Schreurs, Morphology of the Beaufort, Chukchi and Bering Seas nearshore ice conditions by means of satellite and aerial remote sensing: final report, Research unit 257, Geophysical Institute, University of Alaska Fairbanks, Fairbanks, Alaska, 1978.
- Stringer W. J., S. A. Barrett, L. K. Schreurs, Nearshore Ice Conditions and Hazards in the Beaufort, Chukchi and Bering Seas, Report of Geophysical Institute, University of Alaska, Fairbanks, AK, USA, 130 pages, 1980.
- 30 Sun Y., Automatic ice motion retrieval from ERS-1 SAR images using the optical flow method, *International Journal of Remote Sensing*, v. 17, n. 11, pp. 2059–2087, 1996.
- Thomas M., Geiger, C. A., and Kambhamettu, C., High resolution (400 m) motion characterization of sea ice using ERS-1 SAR imagery, *Cold Regions Science and Technology*, v. 52, n. 2, pp. 207–223, 2008.
- Weeks W. F., *On Sea Ice*, University of Alaska Press, Fairbanks, Alaska, USA, ISBN 978-1-60223-101-6, 2010.
- 35 Wessel P., W. H. F. Smith, A Global Self-consistent, Hierarchical, High-resolution Shoreline Database, *Journal of Geophysical Research*, v. 101, n. B4, pp. 8741-8743, DOI: 10.1029/96JB00104, 1996.
- WMO, WMO Sea-Ice Nomenclature, World Meteorological Organization, Report No.259, available online: http://www.jcomm.info/index.php?option=com_oe&task=viewDocumentRecord&docID=14598, 2015.

Yu Y. L., H. Stern, C. Fowler, F. Fetterer, J. Maslanik, Interannual variability of Arctic landfast ice between 1976 and 2007, *J. Clim.*, v. 27, n. 1, pp. 227–243, doi:10.1175/JCLI-D-13-00178.1, 2014.

Zubov N. N., *Arctic Ice*, translated from the Russian original “*Ledy Arktiki*” (Moscow, 1945), U.S Navy Electronics Laboratory, 1960.

Table 1. Comparison of the FMI methods to AARI ice charts, the numbers are in percents. The values in parentheses are standard deviations in percentage points of the AARI ice chart LFI.

Method	Detected (%)	False detection (%)
FMI-A	73.1 (8.8)	20.9 (11.8)
FMI-B	50.4 (13.2)	4.3 (2.2)

Figure Captions

Figure 1. The study area in the used polar stereographic projection.

Figure 2. SAR mosaics of March 8, 2016, HH mosaic (a) and HV mosaic (b). The land areas appear as green and areas of no data as black in the figures.

- 5 Figure 3. Block diagram of the LFI detection (FMI-A) for SENTINEL-1 HH polarization channel. The process for the HV channel is similar, except a threshold value of T_{HV} is applied instead of T_{HH} .

Figure 4. Mask used to locate the areas where LFI is searched. White areas indicate the LFI search area, green areas are land.

Figure 5. The total number of erroneously classified pixels as a function of the temporal cross-correlation average for HH channel SAR data (a) and for HV channel SAR data (b). The optimal thresholds were defined as the minimum of the total error

- 10 (“sum” curves according to the figures legend).

Figure 6. AARI ice chart of March 8, 2016, translated to the polar stereographic projection used in this study and cropped to the study area.

Figure 7. LFI extent based on AARI ice chart (a), FMI-A LFI (b) and FMI-B LFI (c) of March 8, 2016. LFI areas are the black areas in the figures.

- 15 Figure 8. Monthly detection and false detection percentages for LFI-A (a) and LFI-B (b) compared to AARI ice chart LFI, and the relative amount of (AARI) LFI points (c) in percents of the LFI points of the whole year.

Figure 9. Ice extent time series of AARI ice charts, FMI-A and FMI-B during the one-year period from November 1 2015 until October 31, 2016. The time series is weekly with FMI-A and FMI-B for the same days as the weekly AARI ice charts.

Figure 10. FMI-A (a) and FMI-B (b) LFI time series for the whole study period from October 15 2015 until August 31 2017.

- 20 Also the time series of Kara Sea sub-regions, southwestern (SW), northeastern (NE) and Gulf of Ob (Ob) have been included in the figures.

Figure 11. Temporal LFI coverage (percentage) during the period from November 1 2015 until October 31 2016 based on the weekly AARI ice charts (a), daily FMI-A (b) and daily FMI-B (c).

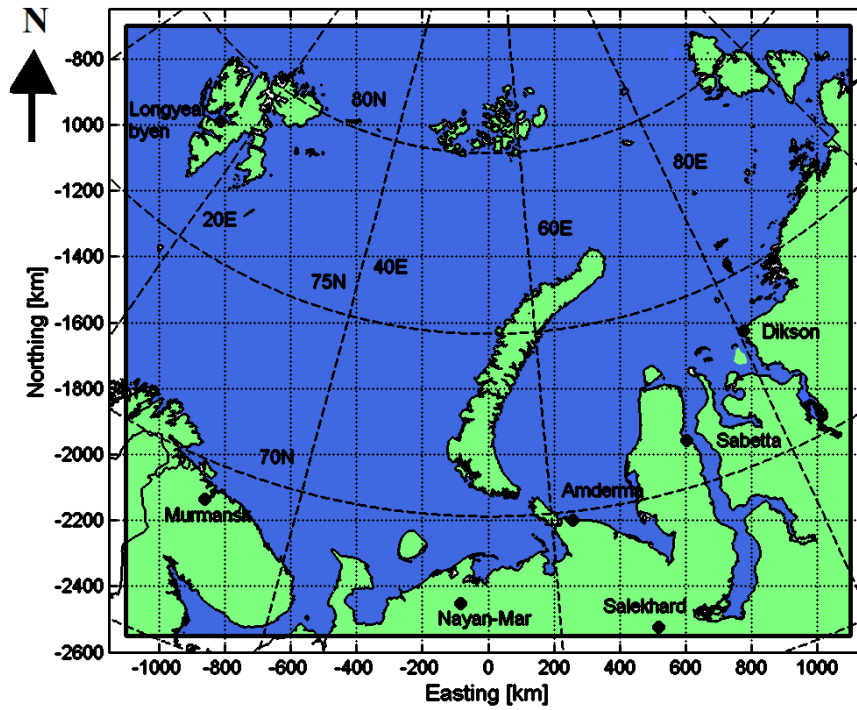


Figure 1. The study area in the used polar stereographic projection.

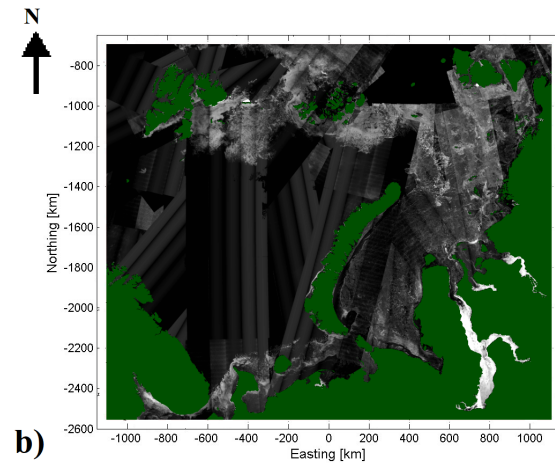
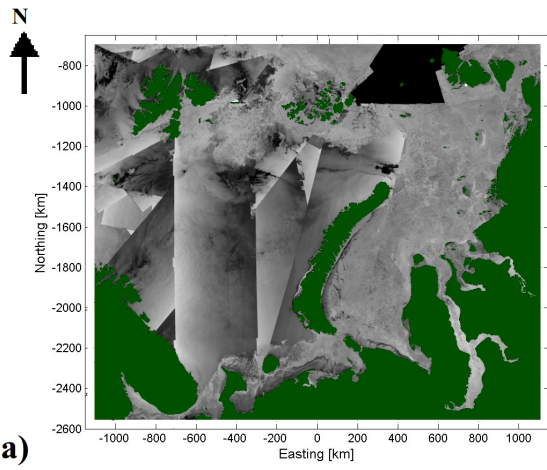


Figure 2. SAR mosaics of March 8, 2016, HH mosaic (a) and HV mosaic (b). The land areas appear as green and areas of no data as black in the figures.

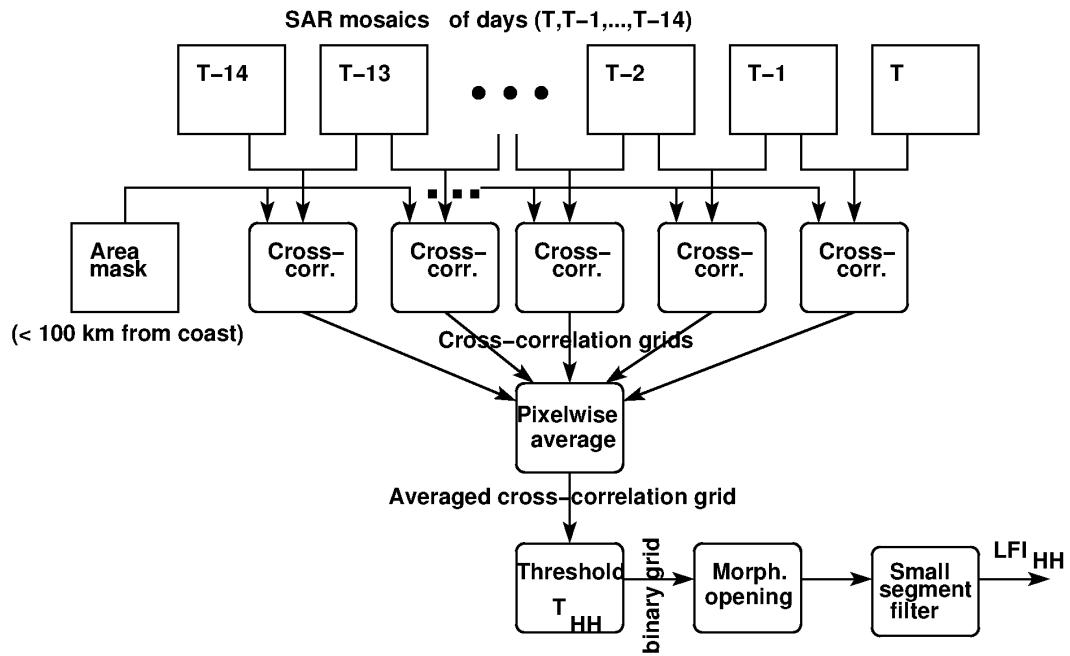


Figure 3. Block diagram of the LFI detection (FMI-A) for SENTINEL-1 HH polarization channel. The process for the HV channel is similar, except a threshold value of T_{HV} is applied instead of T_{HH} .

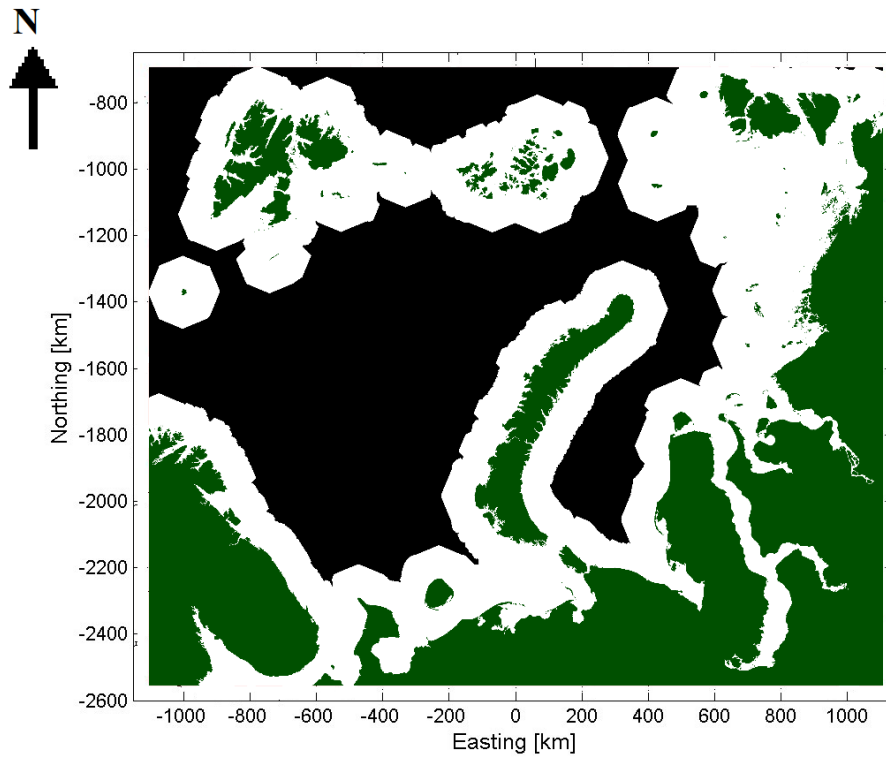


Figure 4. Mask used to locate the areas where LFI is searched. White areas indicate the LFI search area, green areas are land.

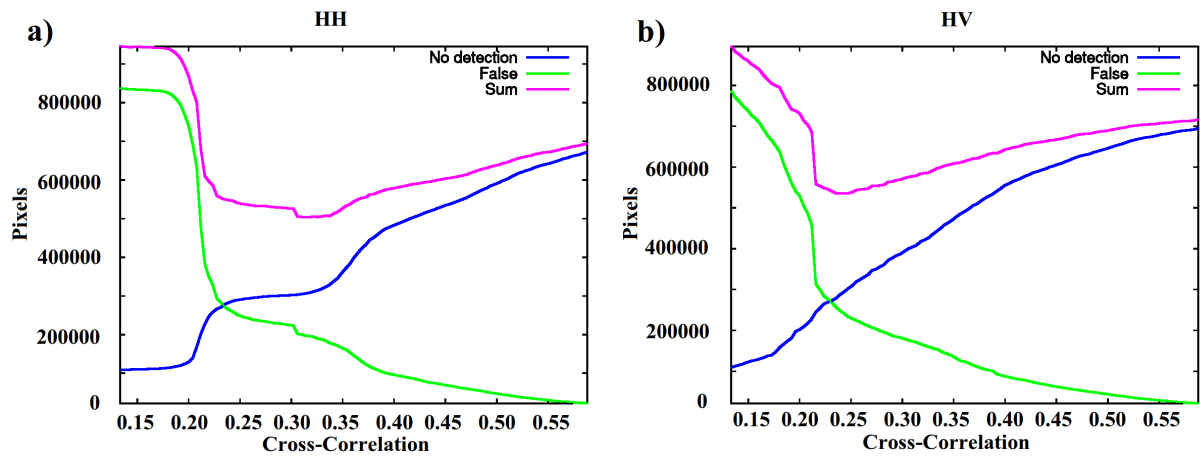


Figure 5. The total number of erroneously classified pixels as a function of the temporal cross-correlation average for HH channel SAR data (a) and for HV channel SAR data (b). The optimal thresholds were defined as the minimum of the total error (“sum” curves according to the figures legend).

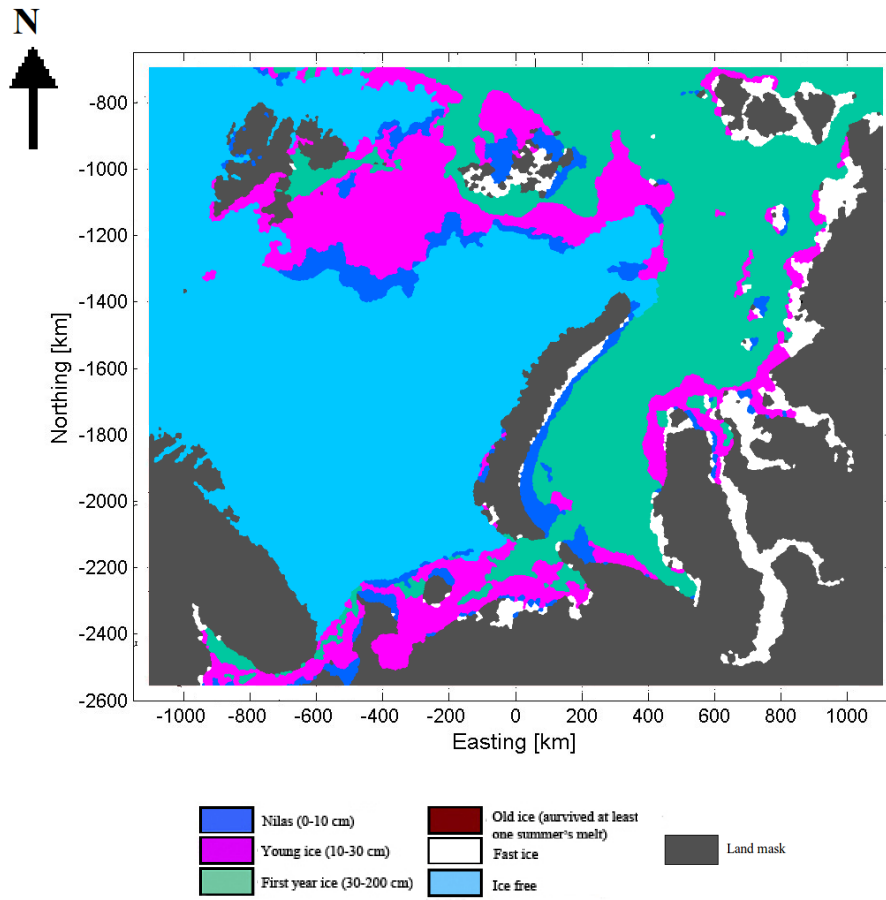


Figure 6. AARI ice chart of March 8, 2016, translated to the polar stereographic projection used in this study and cropped to the study area.

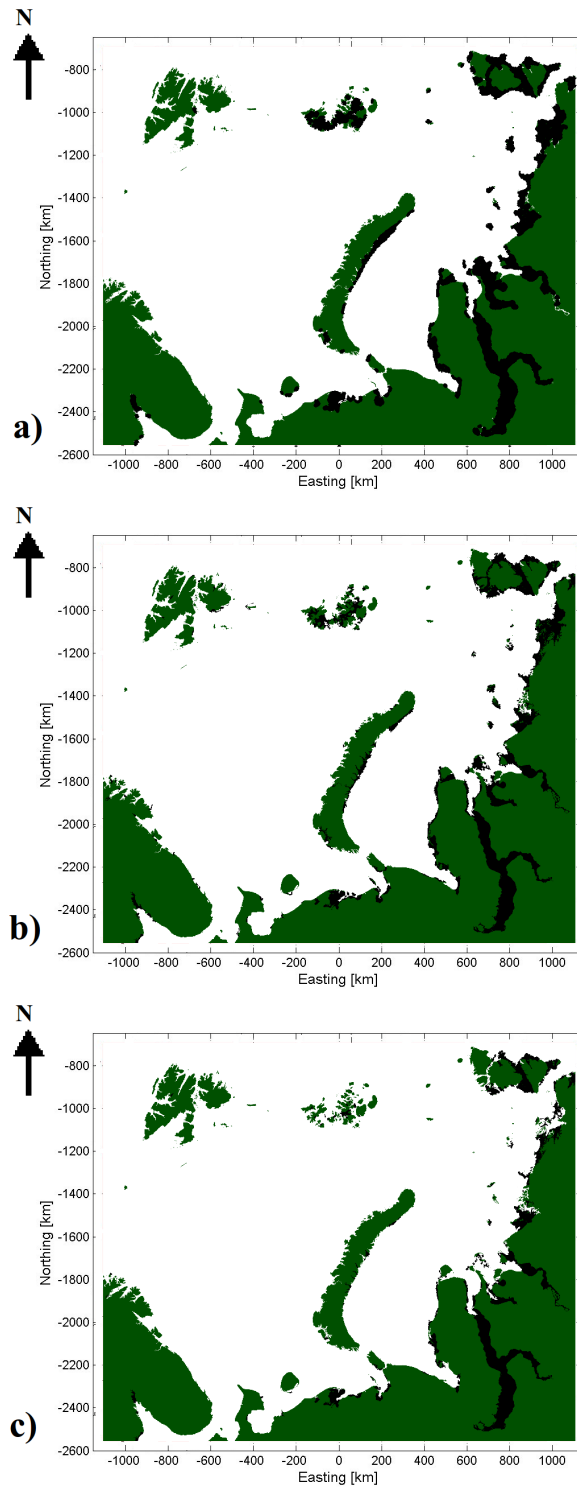


Figure 7. LFI extent based on AARI ice chart (a), FMI-A LFI (b) and FMI-B LFI (c) of March 8, 2016. LFI areas are the black areas in the figures.

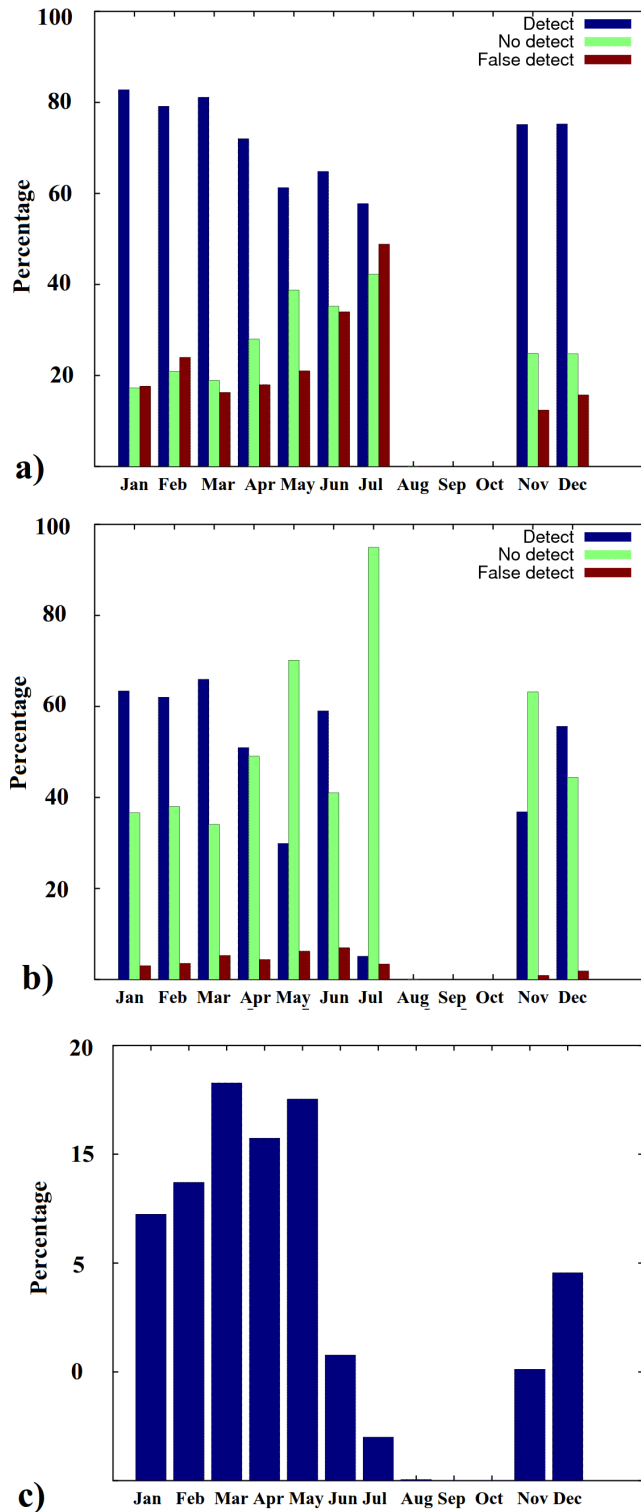


Figure 8. Monthly detection and false detection percentages for LFI-A (a) and LFI-B (b) compared to AARI ice chart LFI, and the relative amount of (AARI) LFI points (c) in percents of the AARI LFI points of the whole year.

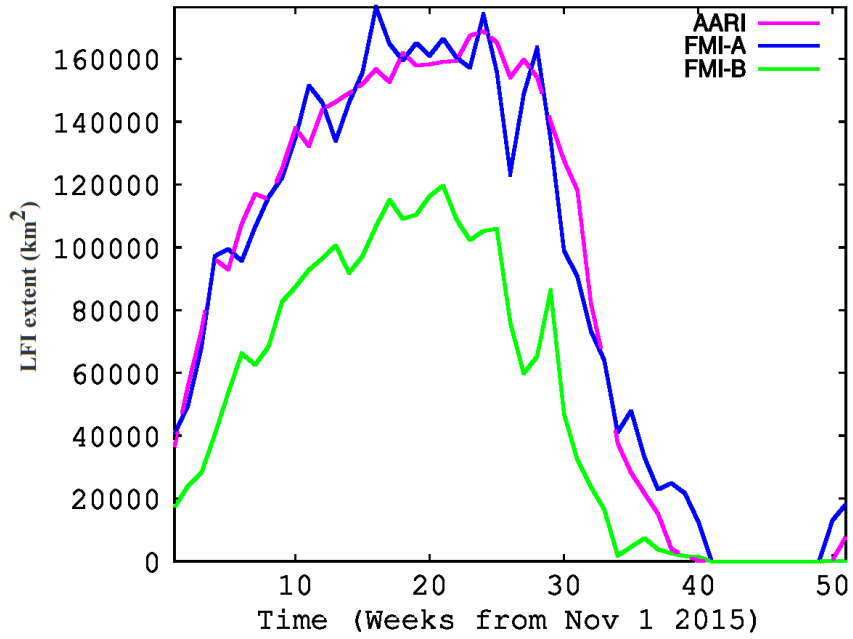


Figure 9. Ice extent time series of AARI ice charts, FMI-A and FMI-B during the one-year period from November 1 2015 until October 31, 2016. The time series is weekly with FMI-A and FMI-B for the same days as the weekly AARI ice charts.

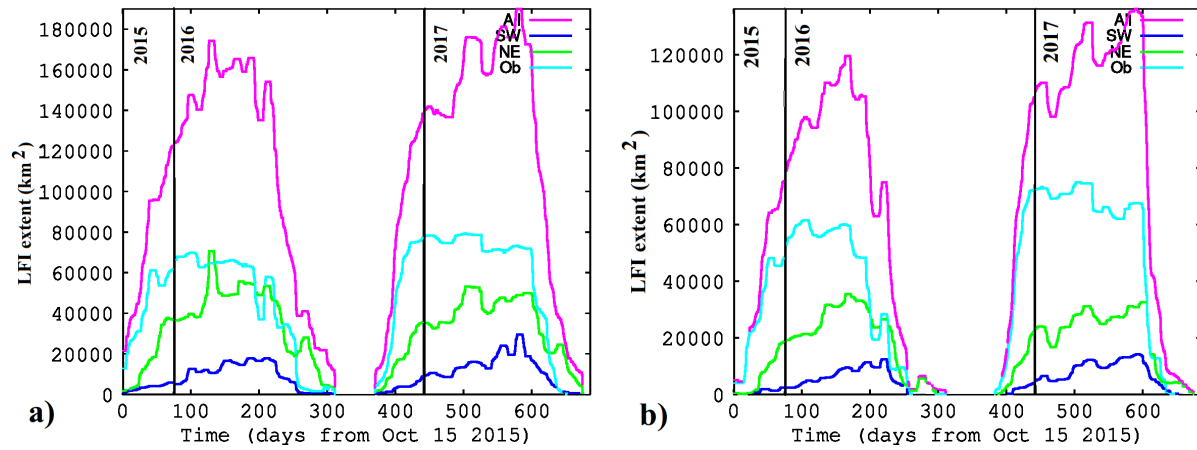


Figure 10. FMI-A (a) and FMI-B (b) LFI time series for the whole study period from October 15 2015 until August 31 2017. Also the time series of Kara Sea sub-regions, southwestern (SW), northeastern (NE) and Gulf of Ob (Ob) have been included in the figures.

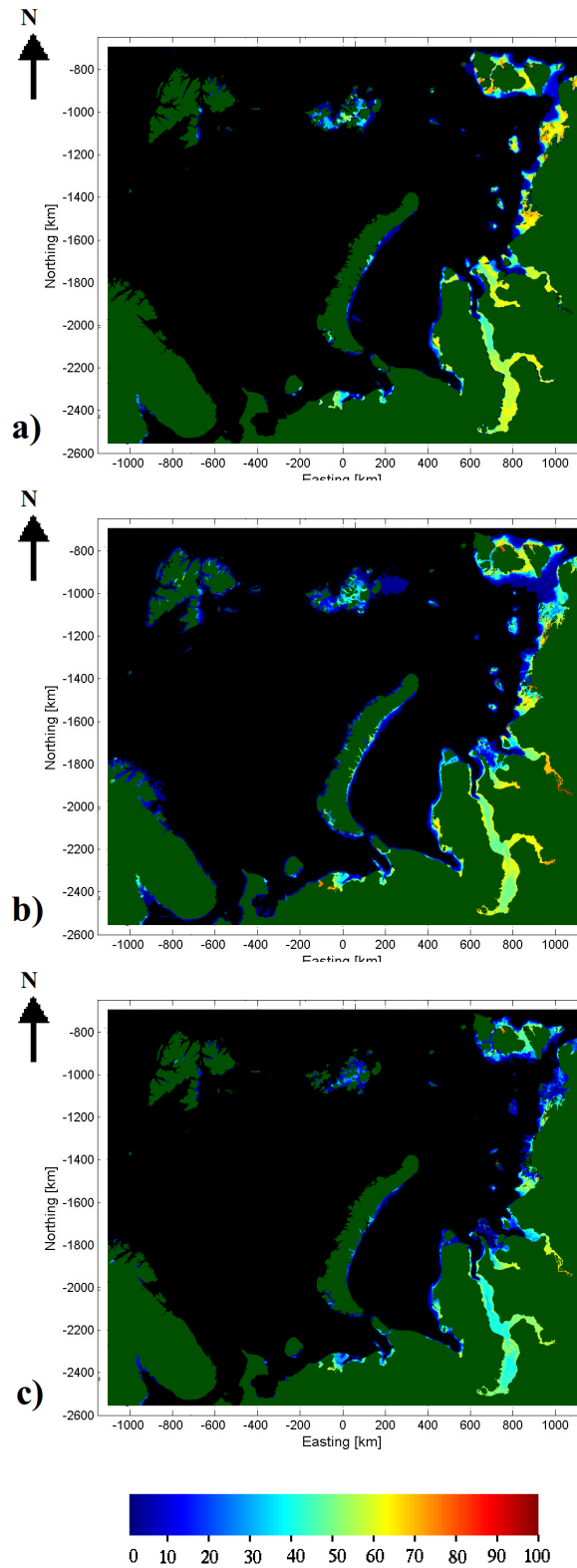


Figure 11. Temporal LFI coverage (percentage) during the period from November 1 2015 until October 31 2016 based on the weekly AARI ice charts (a), daily FMI-A (b) and daily FMI-B (c).